European Polymer Journal 238 (2025) 114211

Contents lists available at ScienceDirect

European Polymer Journal

journal homepage: www.elsevier.com/locate/europolj

Dual thermo- and ROS-responsive triblock copolymers as ^{19}F MRI tracers for functional nanoparticles and hydrogels☆

Fatma Nalan Cetin [a,b], Zulfiya Cernochova [c,*], Edward Vermeersch [a], Vit Herynek [d], Ondrej Groborz [e,f], Ewa Pavlova [c], Miroslav Slouf [c], Martin Hruby [c], Arn Mignon [b], Richard Hoogenboom [g], Sandra Van Vlierberghe [a,*], Kristyna Kolouchova [a,*]

[a] Polymer Chemistry and Biomaterials Group, Centre of Macromolecular Chemistry (CMaC), Department of Organic and Macromolecular Chemistry, Ghent University, Krijgslaan 281, S4, 9000 Ghent, Belgium
[b] Smart Polymeric Biomaterials Group, Department of Materials Engineering, KU Leuven, Andreas Vesaliusstraat 13, 3000 Leuven, Belgium
[c] Institute of Macromolecular Chemistry, Czech Academy of Sciences, Heyrovskeho Namesti 1888/2, 162 00 Prague 6, Czech Republic
[d] Center for Advanced Preclinical Imaging (CAPI), First Faculty of Medicine, Charles University, Salmovská 3, 120 00 Prague, Czech Republic
[e] Institute of Organic Chemistry and Biochemistry, Czech Academy of Sciences, Flemingovo sq. 2, 160 00 Prague, Czech Republic
[f] Institute of Biophysics and Informatics, First Faculty of Medicine, Charles University, Salmovská 1, 120 00 Prague, Czech Republic
[g] Supramolecular Chemistry Group, CMaC, Department of Organic and Macromolecular Chemistry, Ghent University, Krijgslaan 281, S4, 9000 Ghent, Belgium

ARTICLE INFO

Keywords:
Thermogelling
Nanogels
Theranostics
Poly[*N*-(2,2-difluoroethyl)acrylamide]
Poly(2-ethyl-2-oxazoline)
Drug Delivery Systems

ABSTRACT

Theranostic systems that integrate therapeutic delivery with diagnostic imaging hold strong potential in biomedical applications. Nanocarriers with imaging and controlled release functions enable real-time tracking and localization of therapeutics, while hydrogels with diagnostic capabilities support applications such as sustained drug release, cell encapsulation, and cell tracking. Fluorine-19 magnetic resonance imaging (^{19}F-MRI) is a promising non-invasive complement to conventional proton MRI, though its clinical translation remains limited by the lack of optimal tracer systems. Herein, we report the development of BAB-type triblock copolymers comprising a hydrophilic poly(2-ethyl-2-oxazoline) (PEtOx) A block and a thermoresponsive poly[*N*-(2,2-difluoroethyl)acrylamide] (PDFEA) B block, statistically copolymerized with a ROS-responsive monomer bearing phenylboronic ester groups. These polymers self-assemble into nanoparticles at low concentrations and form thermogelling hydrogels at higher concentrations, allowing for formulation-dependent versatility. The ROS-sensitive component enables disassembly at pathophysiologically relevant ROS levels (~0.4–2 mM), facilitating targeted therapeutic release in oxidative environments such as tumors. The polymers form physically crosslinked nanogels (hydrodynamic radius ≈160–760 nm) at 37 °C, which undergo ROS-triggered disassembly. Selected formulations demonstrated excellent ^{19}F-MRI relaxation properties suitable for *in vivo* imaging. Cytocompatibility was confirmed *in vitro* using human foreskin fibroblasts. Overall, the developed polymers offer a versatile platform for biomedical applications—ranging from thermogelling injectable hydrogels for drug delivery or cell encapsulation, to nanocarriers for ROS-triggered therapeutic release—all while enabling non-invasive monitoring via ^{19}F-MRI.

1. Introduction

Theranostics, which integrate therapeutic and diagnostic capabilities, have emerged as a highly promising approach, particularly in the field of cancer treatment [1]. This dual functionality allows for early diagnosis, precise molecular imaging, targeted therapy exploiting optimal dosages at selected time points, and real-time monitoring of the therapeutic efficacy [2]. A notable subset of theranostics involves

---

☆ This article is part of a special issue entitled: ‘Poly(2-oxazoline)s’ published in European Polymer Journal.

* Corresponding authors.

E-mail addresses: fatmanalan.cetin@ugent.be (F.N. Cetin), cernochova@imc.cas.cz (Z. Cernochova), edward.vermeersch@ugent.be (E. Vermeersch), vit.herynek@lf1.cuni.cz (V. Herynek), ondrej.groborz@seznam.cz (O. Groborz), pavlova@imc.cas.cz (E. Pavlova), slouf@imc.cas.cz (M. Slouf), mhruby@centrum.cz (M. Hruby), arn.mignon@kuleuven.be (A. Mignon), richard.hoogenboom@ugent.be (R. Hoogenboom), sandra.vanvlierberghe@ugent.be (S.V. Vlierberghe), kristyna.kolouchova@ugent.be (K. Kolouchova).

https://doi.org/10.1016/j.eurpolymj.2025.114211
Received 31 May 2025; Received in revised form 7 August 2025; Accepted 8 August 2025

nanocarrier-based systems that incorporate both a diagnostic component and an encapsulated therapeutic agent. The inclusion of a diagnostic modality offers the significant advantage of correlating therapeutic outcomes with the presence of the nanocarrier or the administered drug at the tumor site [3].

Magnetic resonance imaging (MRI) is a widely used, non-invasive medical imaging technique. Its importance in medicine has been growing, especially following FDA's Center for Devices and Radiological Health, which started an initiative to minimize unnecessary radiation exposure from medical imaging [4]. Conventional ^{1}H-MRI offers many advantages such as high-resolution anatomical imaging of soft tissues and no limitation regarding sample penetration. However, MRI has its limitations, namely that many pathologies have similar MR properties to those of surrounding tissues, rendering them difficult to distinguish from one another [5,6]. Although paramagnetic contrast agents can enhance contrast, they often come with drawbacks, including potential toxicity and restricted biodistribution [7]. As an alternative method to broaden the scope of MRI, the detection of fluorine-19 in MRI (^{19}F-MRI) has gained increasing attention. Natural fluorine is monoisotopic (only ^{19}F) and this nuclide exhibits magnetic resonance (MR) sensitivity similar to that of ^{1}H. Additionally, the natural abundance of ^{19}F in the human body is minimal, as it is predominantly found in bones and teeth. These tissues are not typically accessible through MRI visualization since fluorine here is present in the form of fluoroapatite with inappropriate relaxation properties for MRI, so natural background is close to zero [8]. The adaptation of conventional ^{1}H-MRI scanners for ^{19}F-MRI requires only minor modifications, enabling its practical integration into clinical settings for so-called dual imaging (^{1}H-^{19}F MRI) of ^{19}F-containing tracers [9]. Despite these advantages, the broader application of ^{19}F-MRI is constrained by the limited availability of suitable fluorinated tracers.

Ideal tracers should contain a high fluorine content, exhibit appropriate physico-chemical properties (including magnetically and chemically equivalent fluorine atoms), optimal MR relaxation times (T_1 and T_2), and must be non-toxic, biocompatible, and excretable from the body after fulfilling their task [10,11]. Fluorinated macromolecules have been explored as prominent ^{19}F-MRI tracers [10,12]. Unlike the low-molecular perfluorinated tracers, the biodistribution of polymeric tracers can be tailored, while a high content of chemically equivalent fluorine can also be achieved [11,13]. Recently, a novel macromolecular ^{19}F-MRI tracer, poly[*N*-(2,2-difluoroethyl)]acrylamide (PDFEA), has been developed, with close to ideal properties in terms of ^{19}F MRI [10,11,14]. PDFEA contains 28 wt% magnetically equivalent fluorine atoms, which leads to a single signal in the MR spectrum while the solvation of the fluorine atoms in PDFEA-based self-assembled structures leads to highly suitable ^{19}F-MR relaxation properties [14–16].

In addition, aqueous solutions of PDFEA exhibit lower critical solution temperature (LCST) behavior, meaning that the polymer is soluble in aqueous solutions at temperatures below the LCST, while undergoing phase separation above its LCST [17]. For this reason, PDFEA copolymers can self-assemble into well-defined supramolecular nanocarriers, while retaining ^{19}F-MRI detectability. Depending on the architecture and chemical nature of their building blocks, these polymers can form nanoparticles, injectable implants, or physically crosslinked hydrogels [10]. This structural versatility makes PDFEA copolymers highly suitable for a broad range of biomedical applications—from nanocarriers enabling sustained or controlled drug release to potential use in cell encapsulation and labeling for advanced cell therapies [10,18,19].

In the nanoparticle form, PDFEA copolymers can passively target tumor sites for smart drug delivery when they are loaded with therapeutic compounds [12]. Passive targeting of tumor sites through nanoparticles is a phenomenon explained via the well-known enhanced permeation and retention (EPR) effect, in which nanoparticles of certain sizes accumulate at tumor sites [20]. Passive targeting can be combined with controlled release by introducing reactive targeting moieties that are responsive to relevant stimuli, such as the tumor microenvironment. Once the nanoparticles accumulate at these tumor sites, they are exposed to the physiological conditions of the tumor microenvironment, which differ from those of healthy tissue. It is known [21] that the tumor microenvironment contains larger amounts of reactive oxygen species (ROS), such as hydrogen peroxide, singlet oxygen, and superoxide anions, compared to healthy tissues, which can be exploited as a reactive targeting strategy [22]. This can be achieved by incorporating ROS-responsive moieties, which allow for nanocarrier disassembly upon oxidation, resulting in the controlled release of the encapsulated therapeutic compound at the tumor site [23].

Hydrophilic poly(2-alkyl oxazolines) (PAOx) have emerged as promising candidates to replace polyethylene glycol (PEG) in biomedical applications due to the increasing incidence of anti-PEG antibodies resulting from the overuse of PEG-based detergents in everyday products and PEGylated nanoparticles in COVID-19 vaccines [24]. Structural variation of PAOx leads to the creation of a wide variety of biocompatible polymers [25]. Among these, PEtOx exhibits LCST properties in the range of 60 – 70 °C, depending on the degree of polymerization, polymer concentration, as well as the presence of salts. Hence, it has gained increasing attention in the context of biomedical applications as a biocompatible and hydrophilic polymer applicable at physiologically relevant temperatures [26]. Moreover, PEtOx has been widely used as a hydrophilic corona in nanocarrier systems due to its stealth properties, effectively prolonging circulation time in the bloodstream and reducing recognition by the immune system [27]. In this study, we developed BAB triblock copolymers, where B is a statistical ROS- and thermoresponsive copolymer of DFEA and [4-(*O*-methacryloylaminomethyl) phenylboronic acid pinacol ester] (ROSm), and A is poly(2-ethyl-2-oxazoline) (PEtOx) as hydrophilic block. The ROSm decomposes into polymethacrylic acid in an environment with excessive ROS levels (pathophysiologically relevant H_2O_2 concentrations of approximately 1 mM [24]) [23]. We prepared six triblock copolymers targeting two different hydrophilic-to-hydrophobic block ratios (1:2 and 1:4) and within these two groups, we varied the ROSm content from 1 mol% to 8 mol% with respect to the overall polymer. We determined their ability to self-assemble upon increasing temperature, to physically crosslink into hydrogels following a change in polymer concentration, and their disassembly or reshaping upon exposure to H_2O_2. The cloud point temperature (T_{CP}), morphology, and size of the obtained particles were studied using dynamic light scattering (DLS), static light scattering (SLS), and turbidimetry. The results were compared with data gathered from transmission electron microscopy (TEM). We assessed the suitability of the selected particle systems to serve as fluorinated macromolecular tracers via ^{19}F-MRI, ^{19}F magnetic resonance spectroscopy (MRS), and by evaluating their relaxation properties. Finally, the cytocompatibility of these particle systems was investigated *in vitro* via live/dead assays.

2. Experimental section

2.1. Materials

α,α′-Dibromo-*p*-xylene (initiator), 2-ethyl-2-oxazoline, potassium hydroxide (KOH) (>97 %), ethyl acetate (≥99.7 %, EtOAc), deuterated dimethylsulfoxide (DMSO-d_6, ≥98 %), triethylamine (TEA, ≥ 99 %), acryloyl chloride (99 %, ≈ 400 ppm phenothiazine as stabilizer), methacryloyl chloride (97 %, contains monomethyl ether hydroquinone as stabilizer), Dulbecco's modified Eagle medium (DMEM), 10 v/v% fetal bovine serum (FBS), 1 v/v% penicillin/streptomycin, calcein-acetoxymethyl (Ca-AM), propidium iodide (PI), 4-cyano-4-[(dodecylsulfanylthiocarbonyl)sulfanyl]pentanoic acid (97 %, CTA), 4-(hydroxymethyl) phenyl boronic acid pinacol ester, and 2,2′-azobis(2-methylpropionitrile) (AIBN, 98 %) were purchased from Sigma-Aldrich (Diegem, Belgium). Methanol (MeOH), tetrahydrofuran (THF) and N,N'-dicyclohexylcarbodiimide were purchased from Acros Organics (Geel, Belgium) and dried using conventional procedures before use. CD_3OH

(methanol-d_4, 99.80 % D) was purchased from Eurisotop (Saint-Aubin, France). 2,2-difluoroethylamine (97 %) was acquired from Fluorochem (Derbyshire, UK). Deionized water used in all experiments (resistivity higher than 18.2 MΩ·cm) was prepared using an Arium® 611 (Sartorius, Goettingen, Germany) with the Sartopore 2 150 (0.45 + 0.2 μm pore size) cartridge filter. Chloroform (stabilized with amylene, >99 %), dichloromethane, and diethyl ether (stabilized with 5–7 ppm BHT, >99 %) were supplied by Chem-lab NV (Zedelgem, Belgium). Magnesium sulfate anhydrous was purchased from Carl Roth (Karlsruhe, Germany). Human foreskin fibroblasts (HFFs) were purchased from ATCC (American Type Culture Collection).

2.2. Methods

2.2.1. Synthesis of ROS-responsive oxygen-containing 4-(O-methacryloylaminomethyl) phenylboronic acid pinacol ester monomer (ROSm)

According to a previously described protocol [28], 4-(hydroxymethyl)phenyl boronic acid pinacol ester (8.54 mmol, 2.00 g) was dissolved in anhydrous DCM (30.0 mL), and TEA (10.3 mmol, 1.04 g) was added to the solution at 0 °C. Afterwards, distilled methacryloyl chloride (10.3 mmol, 1.10 g), dissolved in 5.00 mL anhydrous DCM, was added dropwise within approximately1 h while keeping the reaction at 0 °C under fast mechanical stirring and an argon atmosphere. Then, the reaction was left at room temperature under continuous stirring for 7 h. The product was washed with brine thrice, dried over anhydrous $MgSO_4$, and filtered prior to solvent removal via rotary evaporation. Silica column chromatography was performed using hexane/ethyl acetate (v/v = 9/1) as eluent for purification of the product, followed by solvent removal on a rotary evaporator. ROSm was obtained as a colorless oil with a yield of 2.40 g (77.0 %).

^{1}H NMR characterization (DMSO-d_6): 1.3, (s, 12H, CH_3), 2, (s, 3H, C-CH_3), 5.2, (s, 2H, OCH_2), 5.6, (s, 1H, C=CH_2), 6.1, (s, 1H, C=CH_2), 7.36, (d, 2H, aryl), 7.8, (d, 2H, aryl) (Fig. S1).

2.2.2. Synthesis of bifunctional poly(2-ethyl-2-oxazoline) (PEtOx) macroCTA

All chemicals for the synthesis of PEtOx were purified and dried by distillation under argon (EtOx, EtOAc) or by recrystallization and drying in a desiccator (initiator) and stored in a glovebox (VIGOR Sci-Lab SG 1200/750 glovebox system with a water concentration ≤ 0.1 ppm) under argon atmosphere. The initiator α,α′-dibromo-*p*-xylene (165 mg, 0.625 mmol), EtOx (5.20 mL, 51.5 mmol), EtOAc (7.60 mL, 77.8 mmol), and a stirring bar were added to the polymerization flask in the glovebox under an argon atmosphere and sealed before removing the flask from the glovebox. The polymerization was then let to stir at 80 °C for 25 h (Fig. 1). The polymerization was quenched with 3.0 equivalents of CTA dissolved in 2.0 mL of dry EtOAc after adding 3.6 equivalents of dry TEA, with respect to the molar amount of the initiator. After addition of the CTA·TEA salt, the reaction mixture was let to stir at room temperature overnight. The polymer was purified by precipitation in diethyl ether, which was cooled using liquid N_2. Afterwards, the polymer was dissolved in MeOH and purified by preparative gel chromatography using Sephadex LH-20 and MeOH as the mobile phase. Finally, the collected polymer fractions were dried by rotary evaporation, the polymer was redissolved in water, and freeze-dried to obtain the final product (7.3 g, 66 %). The end-capping degree of PEtOx macroCTA was determined via UV–Vis spectroscopy to be 81 %. ($\lambda = 308$ nm, $\varepsilon = 14.793$ mM^{-1} cm^{-1}; calibration curve $R^2 = 0.999$).

^{1}H NMR characterization (DMSO-d_6): 1 (3H, $\mathbf{CH_3}$), 2.3 (2H, CH_3-$\mathbf{CH_2}$), 3.4 (4H, N-$\mathbf{CH_2CH_2}$), 1.3 (CTA) (Fig. S2).

2.2.3. Synthesis of N-(2,2-difluoroethyl)-acrylamide (DFEA) monomer

As described in our previous study [14], 2,2-difluoroethylamine (7.50 mL, 8.62 g, 106 mmol) and triethylamine (TEA, 18.2 mL, 13.2 g, 130 mmol) were dissolved in dry tetrahydrofuran (THF, 500 mL) at 0 °C, in a water/ice bath. Acryloyl chloride (10.7 mL, 11.9 g, 132 mmol) was dissolved in dry THF (10 mL), and added dropwise to the TEA/DFEA solution under vigorous stirring at 0 °C. Afterwards, the reaction mixture was left to stir at room temperature for 7 h. The reaction mixture was then filtered through a borosilicate glass buchner filter under vacuum, and the filtrate was diluted with diethyl ether (500 mL). The diluted filtrate was washed three times with an aqueous $NaHCO_3$ solution, and three times with saline using a separation funnel. The organic phases were dried over anhydrous $MgSO_4$, the solvent was removed using a rotary evaporator, and the product was purified by chromatography (mobile phase: ethyl acetate/hexane 1:2). The product was obtained as an off-white solid with a yield of 9.05 g (50 %).

^{1}H NMR characterization (DMSO-d_6, 400 MHz): 8.48 (t, $J = 4.9$ Hz, 1H), 6.28 (dd, $J = 17.1$, 10.1 Hz, 1H), 6.14 (dd, $J = 17.1$, 2.2 Hz, 1H), 6.04 (tt, $J = 55.8$, 3.8 Hz, 1H), 5.65 (dd, $J = 10.1$, 2.2 Hz, 1H), 3.57 ppm (tdd, $J = 16.1$, 6.0, 3.9 Hz, 2H) (Fig. S3).

2.2.4. Synthesis of triblock copolymers (P1-P6)

Triblock BAB copolymers were synthesized by Reversible Addition-Fragmentation Chain Transfer (RAFT) polymerization (Fig. 2a). The bifunctional PEtOx macroCTA, DFEA monomer, ROSm, and AIBN initiator were dissolved in anhydrous DMF (Table 1), bubbled with argon for 30 min, and then left to react overnight in an oil bath at 70 °C under continuous mechanical stirring. The reaction mixture was precipitated in diethyl ether, dissolved in water on an ice bath, and freeze-dried to obtain the products as off-white powders. Yields: P1 (488 mg; 81 %), P2 (563 mg; 93 %), P3 (546 mg; 90 %), P4 (425 mg; 81 %), P5 (320 mg; 61 %), P6 (360 mg; 68 %).

^{1}H NMR characterization (P1, P2, P3, P4 and P6 in methanol-d_4, P5 in DMSO-d_6): PEtOx traces at 1 (3H, $\mathbf{CH_3}$), 2.3 (2H, CH_3-$\mathbf{CH_2}$), 3.53 (4H, N-$\mathbf{CH_2CH_2}$); PDFEA traces at 8 (1H, **NH**), 5.7–6.2 (CF_2**H**, t, $J = 56$ Hz), 3.5–3.7 (2H, $\mathbf{CH_2}CF_2H$), 2–2.3 (1H, **CH**CH_2) 1.45–1.9 (2H, CH$\mathbf{CH_2}$), ROSm traces at 1.30–1.39 (12H, $\mathbf{CH_3}$), 1.07–1.16 (3H, $\mathbf{CH_3}$), 5 (2H, O-$\mathbf{CH_2}$), 1.45–1.9 (2H, CH_3C-$\mathbf{CH_2}$), 7.6–7.8 (2H, Ar H), 7.4 (2H, Ar H), along with CTA end-moiety at 1.22. **Integrals P1**: PDFEA trace 5.7–6.2 ppm, CF_2H = **1** (1H), PEtOx trace 3.53 ppm, N-$\mathbf{CH_2CH_2}$ (4H) merged with PDFEA trace 3.5–3.7 ppm, $\mathbf{CH_2}CF_2H$ (2H) = **3.0057**, ROSm traces 7.4 ppm, Ar H = **0.0432** (2H); **P2**: PDFEA trace 5.7–6.2 ppm, CF_2H = **1** (1H), PEtOx trace 3.53 ppm, N-$\mathbf{CH_2CH_2}$ (4H) merged with PDFEA trace 3.5–3.7 ppm, $\mathbf{CH_2}CF_2H$ (2H) = **3.1604**, ROSm traces 7.4 ppm, Ar H = **0.1383** (2H); **P3:** PDFEA trace 5.7–6.2 ppm, CF_2H = **1** (1H), PEtOx trace 3.53 ppm, N-$\mathbf{CH_2CH_2}$ (4H) merged with PDFEA trace 3.5–3.7 ppm, $\mathbf{CH_2}CF_2H$ (2H) = **3.2423**, ROSm traces 7.4 ppm, Ar H = **0.211** (2H); **P4:** PDFEA trace 5.7–6.2 ppm, CF_2H = **1** (1H), PEtOx trace 3.53 ppm, N-$\mathbf{CH_2CH_2}$ (4H) merged with PDFEA trace 3.5–3.7 ppm, $\mathbf{CH_2}CF_2H$ (2H) = **3.7946**, ROSm traces 7.4 ppm, Ar H = **0.0415** (2H); **P5**: PDFEA trace 5.7–6.2 ppm, CF_2H = **1** (1H), PEtOx trace 1 ppm, $\mathbf{CH_3}$ = **2.0161** (3H), ROSm traces 7.4 ppm, Ar H = **0.0779** (2H);); **P6:** PDFEA trace 5.7–6.2 ppm, CF_2H = **1** (1H), PEtOx trace 3.53 ppm, N-$\mathbf{CH_2CH_2}$ (4H) merged with PDFEA trace 3.5–3.7 ppm, $\mathbf{CH_2}CF_2H$ (2H) = **4.271**, ROSm traces

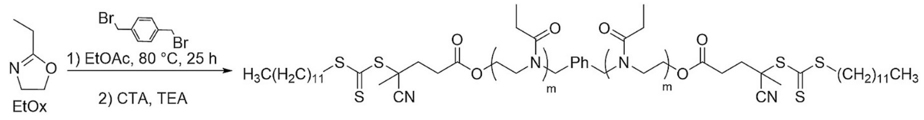

Fig. 1. Synthesis scheme of bifunctional PEtOx macroCTA.

Table 1
Masses and molar amounts of bifunctional macroCTA ($m_{macroCTA}$, $n_{macroCTA}$), DFEA monomer (m_{DFEA}, n_{DFEA}), ROSm monomer (m_{ROSm}, n_{ROSm}), initiator AIBN (m_{AIBN}, n_{AIBN}), and volume of dry DMF (V_{DMF}) used in the RAFT polymerization of BAB triblock copolymers P1-P6.

Polymer	$m_{macroCTA}$ (mg)	$n_{macroCTA}$ (mmol)	m_{DFEA} (mg)	n_{DFEA} (mmol)	m_{ROSm} (mg)	n_{ROSm} (mmol)	n_{AIBN} (mmol)	V_{DMF} (mL)
P1	100	0.019	473.4	3.5	26.6	0.08	0.018	1.3
P2	100	0.019	433.4	3.2	66.6	0.22	0.018	1.3
P3	100	0.019	400.6	3	99.4	0.33	0.018	1.3
P4	150	0.028	356	2.6	19	0.06	0.027	1.3
P5	150	0.028	337	2.5	38	0.12	0.027	1.3
P6	150	0.028	299	2.2	76	0.24	0.027	1.3

7.4 ppm, Ar H = **0.1967** (2H) (Figs. S4-S9).

2.2.5. Size exclusion chromatography

Mass-averaged molecular weight (M_w), number-averaged molecular weight (M_n), and dispersity ($Đ = M_w/M_n$) of the polymers were determined by size exclusion chromatography (SEC) using an Agilent 1260-series high performance liquid chromatography (HPLC) system equipped with a 1260 ISO-pump, a 1260 automatic liquid sampler, a column compartment heated to 50 °C equipped with two PLgel 5 μm mixed-D columns and a precolumn in series, a RI detector and 1260 diode array detector (DAD). The used eluent was dimethylacetamide (DMA) containing 50 mM of LiCl at a flow rate of 0.5 mL/min. Molar mass values and dispersities were calculated against poly(methylmethacrylate) (PMMA) standards. The chromatograms were analysed using Agilent GPC Data Analysis Software (Agilent Technologies, CA, USA,).

2.2.6. Proton nuclear magnetic resonance (^{1}H NMR) spectroscopy

^{1}H NMR spectra (16 scans, 4.1 s acquisition time, 1.0 s relaxation delay) were acquired using a Bruker Avance MSL 400 MHz spectrometer. These spectra were used to determine the polymer purity, block ratios of PDFEA (CHF_2 group of PDFEA, δ = 6.0, 1H corresponds to 1 DFEA unit), PEtOx (CH_2 groups on the backbone, δ = 3.5, 4H correspond to 1 PEtOx unit), and ROSm (aryl CH groups, δ = 7.3, 2H correspond to 1 ROSm unit).

2.2.7. Dynamic light scattering

Intensity-weighted distributions of the hydrodynamic radius (R_H) and scattering intensity of the polymeric assemblies as a function of solution temperature (from 15.0 to 50.0 °C, in increment of 1.0 °C) were measured using a Zetasizer Nano-ZS Malvern instrument (Malvern Instruments, Malvern, UK) with disposable polymethyl methacrylate cuvettes. The excitation light source was a He − Ne laser at 633 nm and the scattered light intensity was measured at an angle of 173°. All polymer solutions (concentration 1.0 mg/mL in 140 mM phosphate saline buffer (PBS), pH 7.4) were kept in the fridge for 15 min and then filtered before measurement using a 0.45 μm PVDF syringe filter. To ensure accuracy, the set points of the temperature values were maintained within ± 0.1 °C. The samples were incubated at each temperature for 500 s before obtaining measurements. An automatic titrator connected to the Zetasizer instrument was utilized to evaluate the ROS-responsive particle disassembly via experiments in which the polymer solutions in PBS were titrated with a series of injections of H_2O_2 solution in PBS at 37 °C while the intensity-weighted distributions of R_H and scattering intensities of the polymeric assemblies were measured via Zetasizer instrument. Five consecutive measurements (titration progress number) for each H_2O_2 concentration were performed starting from 0 until ∼ 3.84 mM as 2 μL injections from a 200 mM H_2O_2 solution were added into the sample cell containing 5 mL polymer solution (1 mg/mL). The data were processed using the Repes algorithm as well as Zetasizer software [29].

2.2.8. Static light scattering

The molecular weight of the particles ($M_{w,p}$) and radius of gyration (R_g) at 25 °C and 37 °C were determined by SLS using ALV-6000 equipment (ALV-GmbH, Langen (Hesse), Germany). For sample P5, the same study was conducted at 25 °C and 35 °C (due to the low stability of the P5 solution at 37 °C). The z-averaged radius of gyration of particles, $\langle R_g \rangle_z$, and the molecular weight, $M_{w,p}$ were obtained from measurements at a range of scattering angles (30° to 149°, increment 4°) and polymer concentrations (0.66, 0.71, 0.76, 0.83, 0.9, and 1 mg/mL in 140 mM PBS, pH 7.4). All samples were filtered using a 0.45 μm PVDF syringe filter. SLS was measured three times and the SLS acquisition time was 40 sec. Subsequently, we constructed a Zimm plot (sample P3 at 25 °C, and P5 at 35 °C), a Guinier plot (P4 both at 25 and 37 °C), and a Berry plot (P3 at 37 °C, and P5 at 25 °C) from the obtained data and analyzed them by the ALV/static and Dynamic FIT and PLOT 4.31 10/01 software (Langen/Hessen, Germany).

In addition, we measured the differential refractive index (dn/dc) using a Brookhaven Instruments Differential Refractometer, followed by analysis through Brookhaven Refractometer Software Ver. 5.32 at different polymer concentrations (0.08, 0.2, 0.4, and 1 mg/mL in 140 mM PBS) and temperatures of 25 and 37 °C.

The densities of the particles (ρ) were calculated using Eq. (1) [30],

$$\rho = M_{w,p}/N_A\left(\frac{4}{3}\right)\pi R_g^3 \tag{1}$$

where N_A is Avogadro's number.

2.2.9. Turbidimetry

Turbidimetry was performed using a Crystal16™ parallel crystallizer turbidimeter (Avantium Technologies, Ontario, Canada) connected to a recirculation chiller and dry compressed air. Aqueous polymer solutions were heated from 10.0 °C to 80.0 °C at a heating rate of 0.5 °C/min, followed by cooling to 10 °C and maintaining this temperature for 30 min. Each measurement was repeated 6 times; the samples were stirred at 700 rpm. All polymers were dissolved in ultrapure water, and phosphate buffered saline (PBS, 140 mM, pH = 7.40) at a concentration of 2.5, 5.0, 10.0, 25, 50, and 100 mg/mL. The samples with polymer concentrations of 100 mg/mL were prepared via addition of water to the polymer in the vial and then they were left to dissolve in the fridge overnight. The lower concentrations were prepared by serial dilutions of the 100 mg/mL solutions. The samples were stored at 4 °C prior to the measurements. Transmittance was monitored at λ = 600 nm. The cloud point temperature (T_{CP}) was determined from the point at which the transmittance dropped below 50 % [31].

2.2.10. Transmission electron microscopy

The morphology of the nanoparticles was visualized using a TEM microscope (Tecnai G2 Spirit Twin 12; FEI Company, Brno, Czech Republic) equipped with a cryogenic sample holder (Gatan, CA, USA). The selected polymers P3, P4, and P5 at a polymer concentration of 1.0 mg/mL in water were characterized after application of our fast-solvent-removal protocol and negative staining with uranyl acetate [32,33]. The fast-solvent-removal protocol, which fixes the morphology of the samples (based on the assumption that the solvent removal is faster than a possible desctruction of nanoparticle morphology), was applied at two temperatures of 5 °C and 39 °C.

The fast solvent removal at 5 °C was performed in three steps: Firstly, the solutions of the selected thermoresponsive polymers (P3, P4, and P5) and tools for sample preparation (microscopic grids, tweezers, tips for micropipettes, etc.) were left to equilibrate in the laboratory refridgerator. Secondly, 2.0 μL of the cooled solutions was deposited on a carbon-coated copper TEM grid and left to evaporate for 1 min (while the sample was still in the refridgerator at 5 °C). Finally, the excess solvent on the grid was removed by touching the bottom of the grid with a small thin strip of filter paper. This fast removal of the solution is a key step in the fast-drying method, which minimizes drying artifacts, as shown in our previous studies [32].

The fast solvent removal at 39 °C was performed in an analogous way as described in the previous paragraph. The only difference was that the samples and all preparation tools were kept in a laboratory oven. The dried samples were equilibrated for at least 1 h in air at room temperature and then they were observed in TEM using bright field imaging at 120 kV.

2.2.11. ^{19}F NMR spectroscopy and relaxation measurements

The T_1 and T_2 relaxation properties of ^{19}F atoms were measured with a Bruker 400 MHz. Both parameters were measured for each sample (polymer concentration of 10 mg/mL in deuterated 140 mM PBS, pH 7.4, at both 25 °C and 37.0 °C). The samples were incubated for at least 15 min at the given temperature before assessment.

The T_1 relaxation time was measured with an inversion recovery experiment (D2 = 0.2 to 3276.8 ms with exponential distribution (two-fold increase). The T_2 relaxation time was measured with CPMG-sequence (D2 = 0.05 ms; n = 4 to 65536) with exponential distributions (two-fold increase). Pulse width of 180° and 90° pulses were optimised before each measurement.

Afterwards, the samples were oxidized using 10 mM H_2O_2 mimicking an oxidative environment, left to react for 24 h and re-measured under identical conditions.

The T_1 and T_2 relaxation properties were determined using a non-linear mixed effect model using custom-made scripts in R (details are provided in the Supplementary Information (SI) of this study; section S6).

2.2.12. ^{19}F magnetic resonance spectroscopy (MRS) and imaging (MRI)

We prepared a set of 18 phantoms with various concentrations (Eppendorf tubes; volume 250 μL; polymer P3-P5 solutions in 140 mM PBS, pH 7.4, at concentrations of 1, 3, 6, 12, 25, and 50 mg/mL). The phantom with the highest concentration (50 mg/mL) was used to acquire ^{19}F-MR spectra at room temperature using a preclinical 7 T scanner (MR Solutions, Guildford, UK) equipped with a ^{1}H/^{19}F dual-frequency whole-body volume coil for rats. A one-pulse FID sequence (bandwidth 50 kHz, repetition time TR = 1000 ms, number of acquisitions NA = 128) was used.

Subsequently, to estimate ^{19}F-MRI detection limit of our setup, all 18 phantoms were measured on ^{1}H and ^{19}F-MRI. We acquired a ^{1}H-MR image using a gradient echo sequence (echo time TE = 4.9 ms, repetition time TR = 200 ms, flip angle FA = 50°, number of acquisitions NA = 4, matrix 256 × 256 pixels, field of view FOV = 64 × 64 mm^2, slice thickness 2.0 mm) and a ^{19}F-MR image using a turbo spin echo sequence (echo spacing TE = 8 ms, turbo factor TF = 4, TR = 500 ms, NA = 128, matrix 64 × 64, FOV = 64 × 64 mm^2, slice thickness 20 mm). Images were recorded at room temperature. Finally, we interpolated ^{19}F images to the same image matrix as was acquired in the case of ^{1}H-MRI (256 × 256), color-coded (red), and merged with ^{1}H images (grey scale) using ImageJ software [34].

2.2.13. In vitro cytocompatibility tests

HFFs were expanded under standard culture conditions (37 °C, 5 % CO_2) in culture medium containing DMEM supplemented with 10 v/v% FBS and 1 v/v% penicillin/streptomycin (P/S). Twice a week the cells were checked and the medium was refreshed.

HFF cells passage 12 were seeded at 10,000 cells per well in a 96 well-plate and cultured overnight under standard culture conditions in culture medium. The following day, the culture medium was removed and 300 μL of the dissolved material was added targeting final concentrations of 0.25 mg/mL, 0.5 mg/mL and 1 mg/mL. A live/dead staining was performed on days 1, 3 and 7 post-incubation to evaluate the cytocompatibility of the materials across different concentrations. On day 1, the staining was performed after removing the polymer-containing solution, however without prior rinsing. This resulted in background fluorescence in some samples, likely due to overlap between the intrinsic fluorescence of the polymer and PI emission spectrum. To minimize this interference, the staining protocol was modified for day 3 and day 7. Prior to staining, all designated wells were rinsed twice with PBS to remove any remaining material. Subsequently, 50 μL of Live/Dead staining solution (1 v/v% Ca-AM in PBS (Merck) / 1 v/v% PI in PBS (Merck)) was added to each well and incubated for 10 min in the dark. Imaging was performed using green fluorescent protein (GFP) and Texas Red (TxRed) filter sets on a fluorescence confocal laser scanning microscope (Carl Zeiss LSM 710, Carl Zeiss AG, Oberkochen, Germany).

3. Results & discussion

3.1. Design, synthesis and characterization of BAB triblock copolymers

The BAB triblock copolymer architecture was selected based on previous reports demonstrating its ability to form nanoparticles at low polymer concentrations and physically crosslinked hydrogels at higher concentrations [14,35]. The developed BAB-type triblock copolymers consist of three components (Fig. 2). The synthesized bifunctional PEtOx macroCTA served as hydrophilic block A in the RAFT polymerization of the BAB triblock copolymers (P1-P6). Among the main classes of CTAs, trithiocarbonates are known to have high transfer constants, cause minimal retardation, and be hydrolytically stable. 4-Cyano-4-[(dodecylsulfanylthiocarbonyl)sulfanyl]pentanoic acid, which was selected as the CTA in this work, is known to be highly compatible with most common monomer types including acrylamides and methacrylates, which were used in this work [36]. In all cases, monomer conversion was between 61 and 93 %. Block B consists of statistical copolymers of PDFEA, being a thermoresponsive polymeric ^{19}F-MRI tracer, and ROS-responsive phenyl boronic acid pinacol ester-based monomer. The PDFEA polymer has been described previously as ideal ^{19}F-MRI tracer capable of thermally induced self-assembly, allowing for the formation of well-defined nanoparticles (Fig. 2b). ROSm has proven effective as ROS-responsive moiety to be exploited in drug delivery studies [28]. At pathophysiologically relevant ROS concentrations (~ 1 mM), benzylic-based boronic esters are oxidized into phenols, which then undergo a quinone methide rearrangement, resulting in a poly(methacrylic acid) unit, leading to a strong hydrophilization of the polymer block. Thus, subsequent particle disassembly and potential cargo release occur due to the substantial reduction of hydrophobic interactions (Fig. 2c). This strategy can be used for controlled drug release in microenvironments exhibiting excessive ROS concentrations such as tumor, inflammation, or chronic wound sites [28,37,38].

In addition, these block copolymers can be designed to have a molecular weight below the renal clearance threshold [39]. Thus, once their function is complete, they can be excreted via the kidneys, while their imaging function enables for tracking to ensure they do not accumulate elsewhere in the body.

In this regard, P1-P6 polymers were prepared to have molar masses below 50 kDa (Table 2), which was determined by SEC. Furthermore, SEC data revealed polymer dispersities ($Đ_M$) between 1.15 and 1.25, indicating that good control over the molar mass has been achieved via RAFT. However, the shoulders present in the SEC traces (Fig. S10) suggest the presence of two molar mass populations, indicating the coexistence of diblock and triblock copolymers. Deconvolution analysis (Fig. S11) revealed that the diblock copolymer constitutes 38–44 % of the material (Table S1). Studies report that the end-group efficiency might reduce due to the chain transfer reactions if the synthesis of the

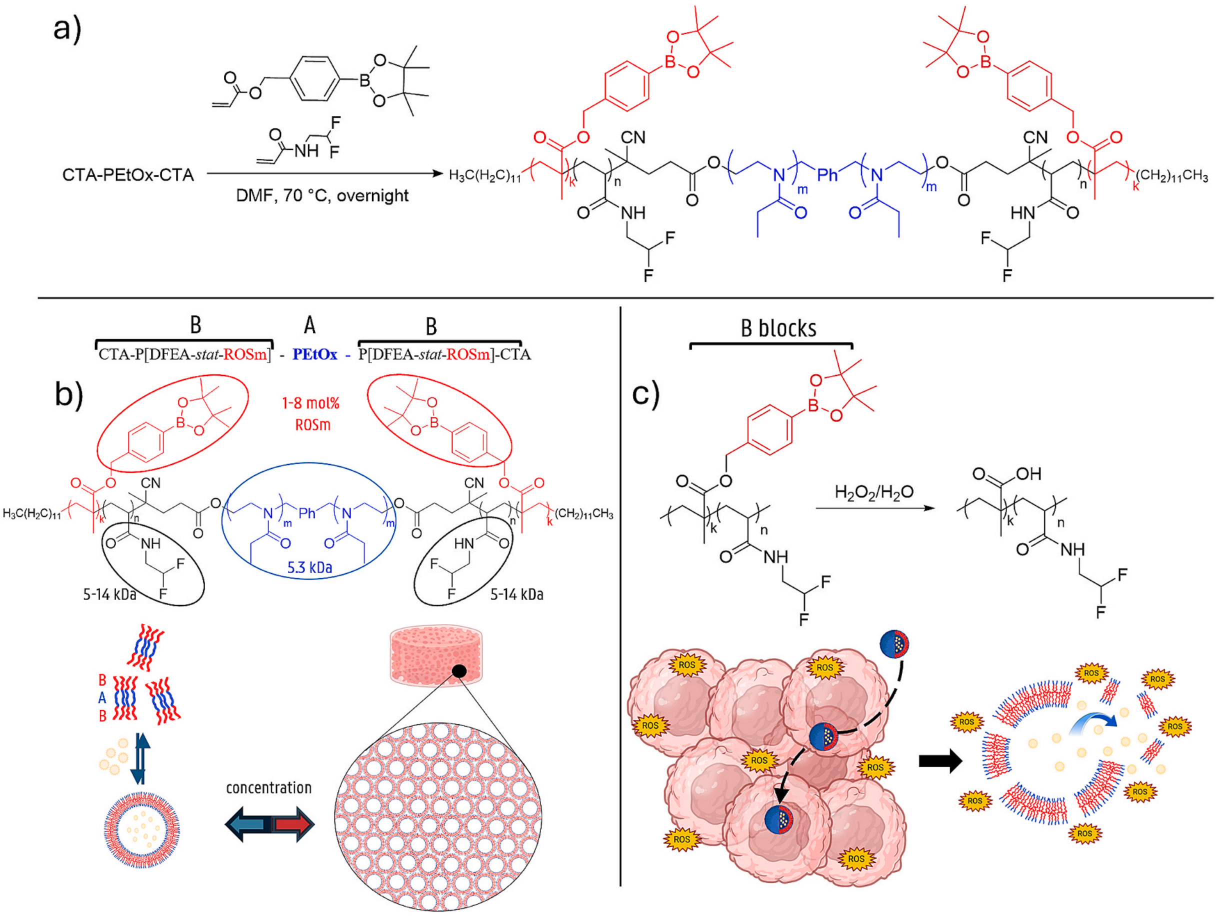

Fig. 2. Scheme displaying the synthesis, concept, and function of the thermo- and ROS-responsive nanoparticle system: a) synthesis scheme and chemical structures of triblock copolymers P1-P6; b) nanoparticle formation from BAB-type triblock copolymers, capable of encapsulating therapeutic cargo and forming physically crosslinked hydrogels upon increased polymer concentration; c) ROS-responsive disassembly of nanoparticles via deprotection of ROSm, exploiting excess ROS as one of the ideal biomarkers characteristic of the tumor microenvironment.

Table 2
Composition and physico-chemical properties of the synthesized bab triblock copolymers: mass average molar mass (M_w), number-average molar mass (M_n), dispersity ($Đ_M$), degree of polymerization (N), mass fraction (f) of PEtOx, PDFEA, and ROSm in block copolymers and mass content of ^{19}F in polymers as weight fraction.

Polymer	M_w (kg/mol)^1	M_n (kg/mol)^1	$Đ_M$ (M_w/M_n) ^{1}	N^2_{PEtOx}	N^2_{PDFEA}	N^2_{ROSm}	f^2_{PEtOx}	f^2_{PDFEA}	f^2_{ROSm}	^{19}F wt%
CTA-PEtOx-CTA	6.1	5.3	1.15	53	0	0.0	1.00	0.00	0.00	0.0
P1	39.6	34.4	1.15	53	211	4.0	0.15	0.82	0.03	23.2
P2	40.1	33.7	1.19	53	183	12.0	0.16	0.74	0.10	20.9
P3	39.5	32.3	1.22	53	171	18.0	0.16	0.68	0.16	19.6
P4	24.1	20.5	1.17	53	118	2.0	0.24	0.73	0.03	21.0
P5	19.4	16.5	1.17	53	79	3.0	0.31	0.63	0.06	18.5
P6	19.8	15.7	1.25	53	93	9.0	0.26	0.61	0.13	17.7

^{1}Determined by SEC; ^{2}Determined by ^{1}H NMR spectroscopy.

PEtOx macroCTA is performed at elevated temperatures as high as ~ 140 °C [40]. Even though the synthesis of the PEtOx macroCTA was performed at 80 °C, we might still observe a similar phenomenon and occurrence of chain transfer side reactions during the cationic ring-opening polymerization. Furthermore, the possible presence of impurities during end-capping, such as traces of water, could further decrease the end-group fidelity. In our study, the end-group functionalization was shown to be 81 %. Future improvements in capping efficiency could potentially reduce diblock formation. Nevertheless, the low dispersity ($Đ_M$) shows the successful synthesis of narrowly distributed copolymers that self-assemble into well-defined nanoparticles, as discussed in the upcoming sections.

As mentioned earlier, the BAB-type block copolymers can self-assemble into nanoparticles and undergo physical crosslinking into hydrogels at higher polymer concentrations. However, this gelation behavior is highly dependent on the specific block ratios. Several studies have explored how BAB-type triblock copolymers with thermoresponsive/hydrophobic outer chains form physically crosslinked hydrogels [14,35,41]. These studies show that hydrogel formation typically requires either low or high A/B block ratios. In one mechanism, copolymers with a long hydrophobic B block (core-forming) and short hydrophilic A blocks (corona-forming) assemble into micelles. As the concentration increases, the hydrophilic end blocks can loop back or bridge between micellar cores, creating physical crosslinks [41]. In another mechanism, where the hydrophilic A blocks are short relative to the thermoresponsive/hydrophobic B block, hydrophobic interactions can drive 'channeling' between neighboring micellar cores [42,43]. These channels act as interparticle bridges, resulting in macroscopic gelation. In both scenarios, the formation of a network is highly dependent on the polymer concentration and nanoparticle number density. To ensure that the BAB copolymers exhibit this transition, we selected specific molecular weight ratios between the blocks. In particular, the molar mass of the thermoresponsive block B was set to be either twice (polymers P1–P3) or four times (polymers P4–P6) that of the hydrophilic block A, similar to ratios reported in previous studies on PDFEA-PEG-PDFEA [14] and poly(2-oxazoline) copolymers [35]. Additionally, ^{1}H NMR spectroscopy was used to determine the degree of polymerization (N), providing insight into the block ratios between PEtOx and PDFEA, and, more importantly, enabling quantification of the molar content of ROSm within block B (Table 2). The total ROSm content varied from 1.5–7.5 mol % and 1.2–5.8 mol % for the polymers P1-P3 and P4-P6, respectively.

3.2. Nanoparticle characterization via light scattering methods

3.2.1. Temperature-dependent particle size and type

The self-assembly of the prepared triblock copolymers P1-P6 was investigated using DLS and SLS (Table 3). Notably, the polymers spontaneously formed nanoparticles in aqueous solutions via direct dissolution, without the need for time-consuming and/or sophisticated techniques such as thin film rehydration, nanoprecipitation, or microfluidics [44].

First, the hydrodynamic radius (R_H) of the particles was measured as a function of temperature using DLS (Fig. 3, Fig. 4, and Fig. 5 & Figs. S12). The results revealed that the samples underwent multiple temperature-induced transitions, also known as cloud point temperatures (T_{CP}s). The initial transition temperature (T_{CP1}) corresponds to the self-assembly of nanoparticles, which occurs when the thermoresponsive B blocks (PDFEA) collapse due to an LCST-type phase transition, forming hydrophobic core. The hydrophilic PEtOx mid-blocks remain solvated, forming a stabilizing corona. The second transition temperature (T_{CP2}) is associated with nanoparticle aggregation and precipitation, likely driven by reduced colloidal stability due to partial dehydration or collapse of the PEtOx corona at higher temperatures, considering its known LCST behavior in the range of ~61–69 °C, as described in related studies with PEtOx-based triblock copolymers [35,45]. Based on these findings, only three samples (P3 to P5) were selected for further studies, as they formed stable nanoparticle solutions at temperatures relevant to physiological conditions.

The temperature-driven self-assembly of polymers P3–P5 is illustrated in Figs. 3–5 and Fig. S12. Values of T_{CP1} (Table 3), at which thermo-responsive self-assembly starts, have been determined from the points where the size of initially formed nanoparticles starts to increase gradually. To further characterize the thermoresponsive behavior above T_{CP1}, SLS measurements were performed at 25 °C and 37 °C. At 25 °C, the samples P3 and P5 exhibited a shape factor of 1.66 and 1.53, respectively (Table 3), indicating the formation of non-spherical nanoparticles, whereas sample P4 exhibited a shape factor of 0.7, indicating a spherical shape, along with a high core density (0.39 g/cm^3), corresponding to spherical micelles. At 37 °C, a transition in particle type was observed. The newly formed particles exhibited properties such as low core density, consistent with the presence of previously reported physically crosslinked nanogels [46,47]. Nanogels are nanoscale, three-dimensional polymer networks that are physically or chemically crosslinked. In aqueous environments, they absorb and retain large amounts of water within their internal network, resulting in a significantly lower core density compared to more compact structures such as micelles or solid polymer nanoparticles. As previously described [12,46], PDFEA-based thermoresponsive systems form self-assembled structures that align with the classic definition of nanogels: thermoresponsive polymer chains form an internal network, surrounded by swollen hydrophilic segments. The hydrophilic domains swell extensively in water, while the thermoresponsive blocks form a denser, physically crosslinked core. The physical crosslinking is primarily driven by the PDFEA blocks, which form strong interchain hydrogen bonding through the –CHF_2 groups and amide functionalities present in each monomeric unit. This leads to the formation of a cohesive and homogeneous polymer network within each particle. The resulting nanogels exhibit substantial swelling in aqueous environments, which accounts for their low core density in comparison to micelles or solid nanoparticles. Additionally, these particles possess a hydrated, hydrophilic corona, which affects interparticle interactions and can promote aggregation, particularly at elevated temperatures.

A second transition occurs at T_{CP2}, where precipitation, i.e., the collapse of overall material, takes place, ascribed to PEtOx (inner block) phase separation. As the temperature window between T_{CP1} and T_{CP2} turned out to be highly narrow in the case of sample P5 (32–37 °C), SLS measurements of this sample were conducted at 35 °C to avoid the onset of aggregation. While we determined that the thermal stability of P5 nanogels remained poor for biomedical applications, we investigated this system for its thermogelling properties, as will be discussed in following sections.

In conclusion, at T_{CP1}, the triblock copolymers appear to form small micellar structures, which then gradually reshape into nanogels as the temperature increases. These smaller structures are present even at temperatures below T_{CP1}, likely due to the amphiphilic nature of the copolymer system. Specifically, the presence of aliphatic end-groups from the chain transfer agent (CTA) and the highly hydrophobic ROSm units in block B contribute to self-assembly below T_{CP1}. The formation of such micellar aggregates below the T_{CP} has also been observed in other thermo-responsive block copolymer systems [14]. Above T_{CP2}, the nanogels tend to aggregate further, leading to a secondary increase in hydrodynamic radius, likely due to the above-mentioned temperature-triggered collapse of the PEtOx inner block. These morphological changes are further supported by TEM analysis

Table 3
Thermo-responsive self-assembly characteristics of P1-P6 solutions (1 mg/mL in PBS) determined via DLS: T_{CP1}, hydrodynamic radii at T_{CP1} and 37 °C, and critical temperature after which the particle systems are not stable (T_{CP2}), along with types of particles determined via SLS measurements at 25 °C and 37 °C (*P5 characterized by SLS at 35 °C).

Polymer	T_{CP1} (°C)^a	R_h (nm) at T_{CP1}^a	R_h (nm) at 37°C^a	T_{CP2} (°C)^a	Shape factor at 25 °C^b	Particle density (g/cm^3) at 25 °C^b	Particle type at 25°C^b	Particle density (g/cm^3) at physiological temperature^b	Particle type at physiological temperature^{b*}
P1	30	624 ± 114	–	36	–	–	–	–	–
P2	20.5	44 ± 14	–	23.8	–	–	–	–	–
P3	19.5	100 ± 0.1	150 ± 2	–	1.66	–	Rod-like nanoparticles	0.07	Spherical nanogels
P4	23	29 ± 3	123 ± 3	43	0.7	0.39	Spherical nanoparticles	0.008	Spherical nanogels
P5	32	37 ± 4		37	1.53	–	Rod-like nanoparticles	0.01	Spherical nanogels
P6	17	37 ± 5	–	21	–	–	–	–	–

^{a}Determined via DLS; ^{b}determined via SLS.

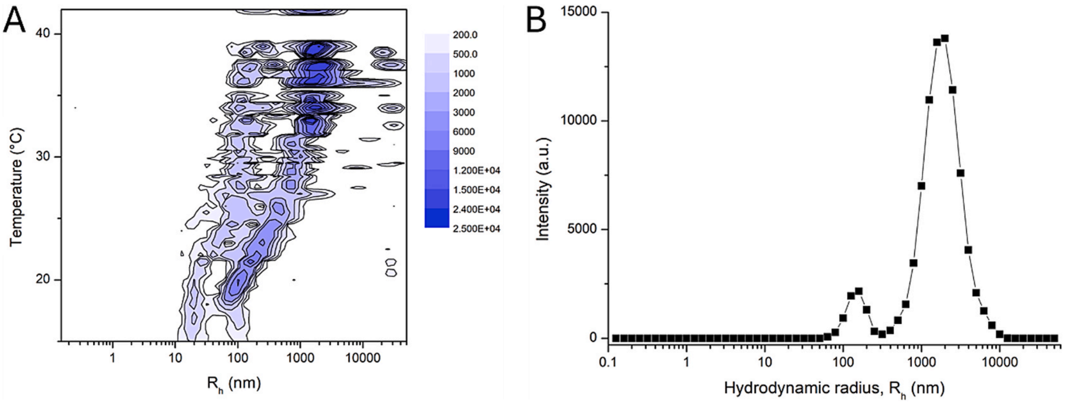

Fig. 3. Scattering intensity weighted hydrodynamic size distributions of polymer P3 solution (1 mg/mL in PBS) characterized by DLS, A) as a function of temperature, or B) at 37 °C.

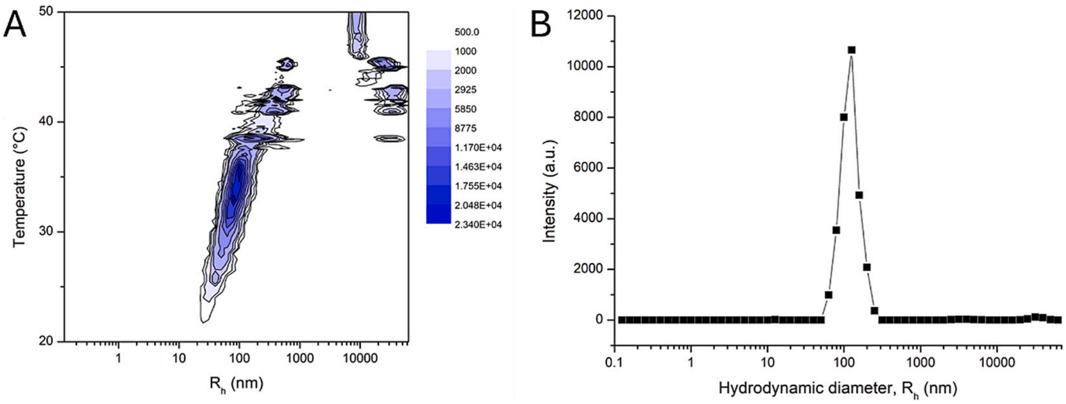

Fig. 4. Scattering intensity weighted hydrodynamic size distributions of polymer P4 solution (1 mg/mL in PBS) characterized by DLS, A) as a function of temperature, or B) at 37 °C.

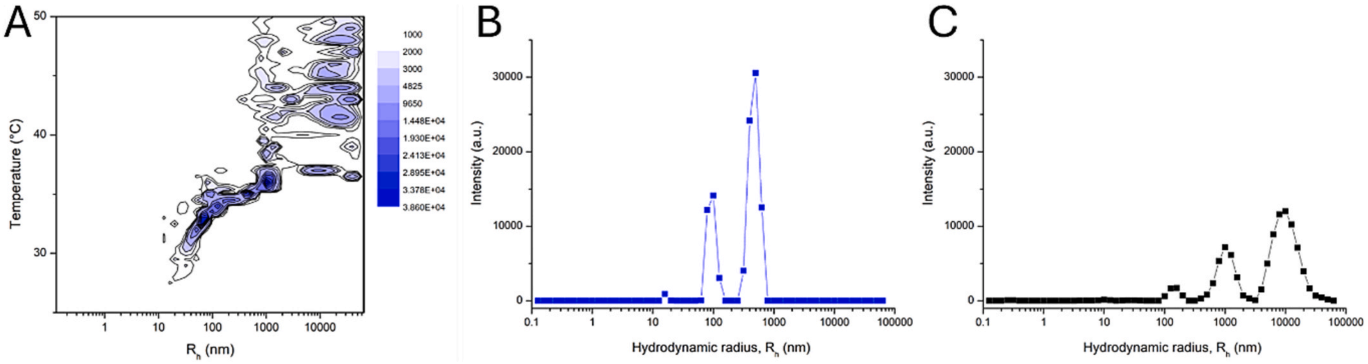

Fig. 5. Scattering intensity weighted hydrodynamic size distributions of polymer P5 solution (1 mg/mL in PBS) characterized by DLS, A) as a function of temperature, B) at 35 °C, or C) at 37 °C.

(Fig. 6), which confirms the presence of both small aggregates at lower temperatures and larger nanogels at elevated temperatures, as described in detail in the next section.

3.3. Nanoparticle characterization via TEM

Polymers P3, P4, and P5 were selected for additional characterization by TEM, as they exhibited temperature-responsive assembly behavior in the physiologically relevant temperature range. To verify the key DLS and SLS results, aqueous solutions of these polymers (1 mg/ml in ultrapure water) were prepared below and above their transition temperature. The morphology of the samples was fixed at two temperatures, 5 °C and 39 °C, using the fast-solvent-removal method, as described in the experimental section. The TEM micrographs (Fig. 6) confirmed the presence of spherical or worm-like particles at very low temperatures, likely below T_{CP1}, and the formation of large nanogels at high temperatures, in alignment with the results from DLS and SLS measurements.

3.4. ROS-induced disassembly of particles characterized via DLS

As described, the ROSm units incorporated in the thermoresponsive

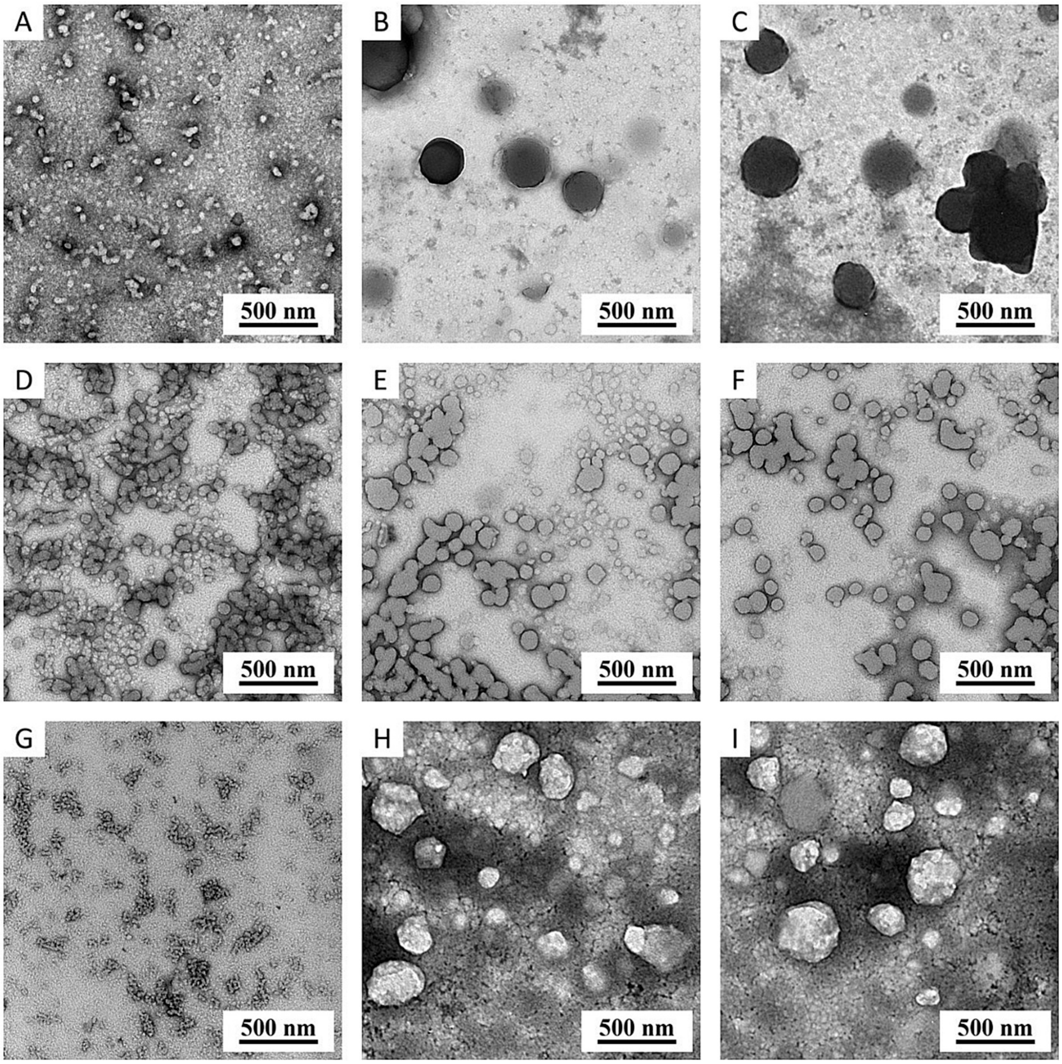

Fig. 6. TEM micrographs of A) P3 (1 mg/mL in ddH_2O) characterized at 5 °C, and B & C) 39 °C; D) P4 (1 mg/mL in ddH_2O) at 5 °C, and E & F) 39 °C; G) P5 (1 mg/mL in ddH_2O) characterized at 5 °C, and H & I) 39 °C.

block are designed to decompose in oxidative physiological environments. To assess the sensitivity of the nanoparticles to oxidative stress within a physiologically relevant range—such as those found in cancerous tissues, sites of inflammation, or chronic wounds—the polymer solutions in PBS were titrated with incremental additions of H_2O_2. The scattering intensity-based hydrodynamic size distributions were analyzed as the H_2O_2 concentration in the samples was incrementally increased from 0 to approximately 4 mM considering the oxidative stress in tissues start at around 0.5 mM and reaches up to 1 mM [48] (Figs. S13–S15). We determined the threshold concentration of H_2O_2 that triggers the decomposition of ROSm and the corresponding change in particle self-association. The determined H_2O_2 concentrations at which the ROS-induced transitions occurred are summarized in Table 4. Additionally, the hydrodynamic radius (R_H) was measured after the transition. The results showed that polymers P3 and P5 were able to form small micelles when the H_2O_2 level reached 0.64 and 0.4 mM, respectively, whereas particle system P4 disassembled around 2 mM H_2O_2. ROS-responsivity of all systems are situated within the pathophysiologically relevant ROS window (≈0.5–1 mM).

Additionally, we evaluated the effect of ROS exposure on the distribution of hydrodynamic sizes in a time-dependent DLS experiment. Polymers P3, P4, and P5 (1 mg/mL solutions) were exposed overnight to 0.1 mM and 10 mM hydrogen peroxide (H_2O_2) solutions in PBS. This range was selected to reflect both low and excessive levels of reactive oxygen species. Lower concentrations of H_2O_2, particularly in the nanomolar range, were deliberately avoided, as these levels are often involved in physiological signaling processes rather than indicating oxidative stress [48]. Therefore, testing within this range provides a more accurate assessment of the nanoparticle response to oxidative environments relevant for therapeutic applications. Fig. 7 shows the case of P3 as an example and reveals that the ROS-responsivity of the particles is more pronounced and immediate under stronger oxidative conditions. All particle systems displayed immediate disassembly upon

Table 4
Threshold concentrations of H_2O_2 that triggers the change in particle self-association upon decomposition of ROSm at 37 °C characterized by a DLS instrument equipped with an automatic titrator.

Sample	Nanogels Initial R_h (nm)	H_2O_2 concentration (mM) at transition point	Transition Type	R_h (nm) of new population at transition point
P3	162	0.64	Micelle formation	37.9
P4	186	2.21	Disassembly	n/a
P5	759	0.4	Micelle formation	22

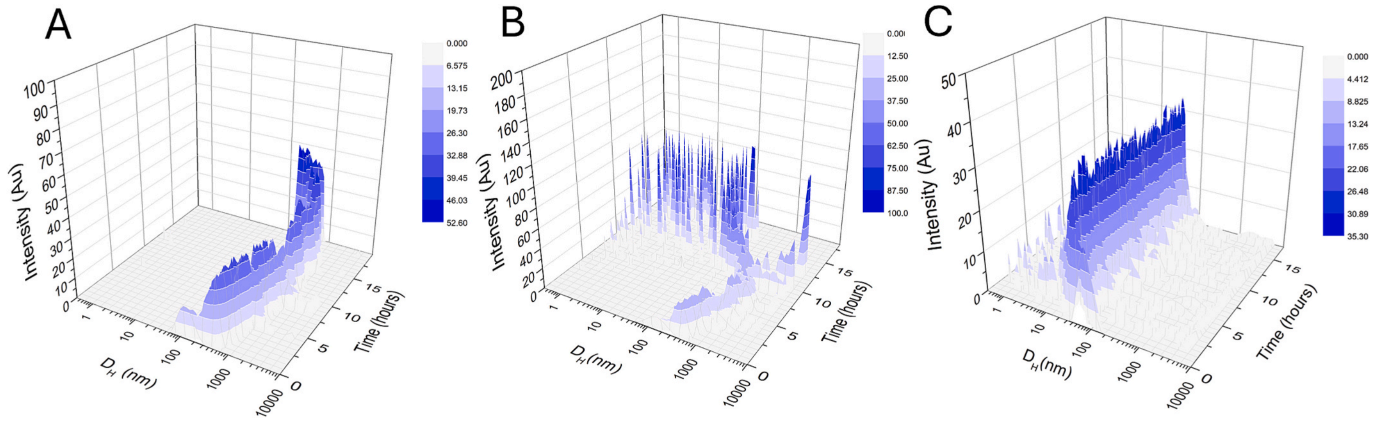

Fig. 7. Scattering intensity based hydrodynamic size distributions of P3 solution (1 mg/mL) in A) PBS, B) 0.1 mM H_2O_2, and C) 10 mM H_2O_2, displaying time-dependent ROS responsivity.

exposure to 10 mM H_2O_2 as the hydrodynamic diameter (D_H) of the main particle populations decreased substantially within 1 h in the case of P3 (Fig. 7) and P5, and after 5 h for P4 (Fig. S16). Following this, populations around $D_H \approx 10$ nm corresponding to free polymer chains appeared. The P3 particle system exhibited a noticeable change in D_H even at 0.1 mM H_2O_2 concentration after 10 h, indicating high sensitivity to ROS. In contrast, polymers P4 and P5 did not exhibit significant changes in particle populations upon exposure to low ROS levels, suggesting their responsiveness is more pronounced under higher oxidative conditions.

3.5. LCST determination via turbidimetry and physical crosslinking at high polymer concentrations

The LCST of the developed copolymers was evaluated via turbidimetry. Cloud point temperatures (T_{CP}s) were assessed across a range of polymer concentrations, as summarized in Fig. 8 (detailed data in Table S2; full turbidimetry measurements are shown in Figs. S17-S22). At higher polymer concentrations (typically above 50 mg/mL), the particles started forming hydrogel networks at the bottom of the vial (Fig. S23), as previously described [14]. This gelation can disrupt stirring and cause local depletion of polymer concentration in the upper part of the solution. Since the turbidimetry laser measures turbidity at the midpoint of the vial, it primarily detects the supernatant above the gel, which no longer reflects the original polymer concentration. For this reason, the cloud point temperature (i.e., temperature at which the transmittance drops to 50 %) at higher concentrations can only be reliably evaluated from the first heating cycle. All subsequent cycles show thermal hysteresis, but the data are less reproducible due to the altered sample state. For samples without hydrogel formation, the cloud point temperatures were determined from all heating cycles and reported as the mean ± standard deviation, as shown in Table S2.

As mentioned earlier, polymers described here are capable of physical crosslinking into hydrogels through a process, where the hydrophilic A blocks are short relative to the thermoresponsive/hydrophobic B block, and hydrophobic interactions can drive 'channeling' between neighboring micellar core [42,43]. These channels act as interparticle bridges, resulting in macroscopic gelation. The effect of polymer concentration on this gelation mechanism can be qualitatively observed from images of turbidimetry vials taken at the end of the experiment, as shown in Fig. S23. Samples P1, P2, P3, and P4 formed hydrogels at the bottom of the vial starting from 25 mg/mL. However, at concentrations below 25 mg/mL, hydrogel formation was not observed. Hydrogels formed by these polymers were not able to swell in aqueous phase, therefore, the hydrogel appears only at the top of the inverted vial, holding the mechanical stirring bar within its structure, while the

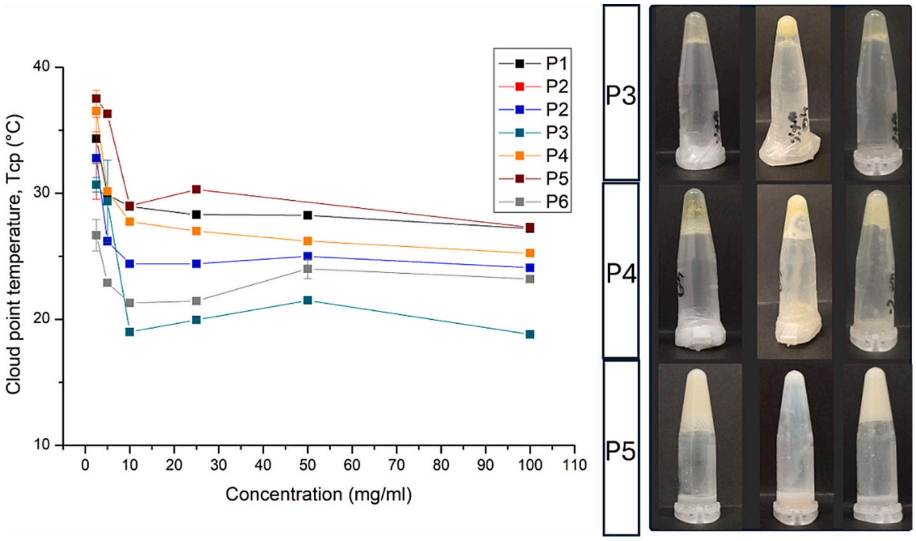

Fig. 8. The plot on the left shows T_{CP} of P1-P6 polymer solutions in PBS at varying polymer concentrations, evaluated from turbidimetry cycles (six heating and cooling cycles between 10–80 °C). The images on the right show hydrogels prepared from 40 wt% polymer solutions (P3, P4, and P5) in PBS at 4 °C (left), after incubation at 37 °C overnight (center), and after exposure to 4 °C overnight (right).

excluded aqueous phase collects at the bottom. On the other hand, P5 formed hydrogels that could swell at 100 and 50 mg/mL concentrations, therefore, no excluded aqueous phase was observed in these cases. As the polymer concentration decreased, hydrogels still formed at concentrations as low as 2.5 mg/mL, but an excluded aqueous phase became visible. This difference may arise from the size of the nanogels. As DLS experiments revealed, P5 creates nanogels with $R_H \approx 760$ nm at 37 °C, while P3 and P4 create nanogels with $R_H \approx 162$ and $R_H \approx 186$ nm, respectively.

Accordingly, the relevant polymers P3-P5 were tested at high concentrations (40 wt%), at which homogeneously physically crosslinked hydrogels formed successfully. Gel formation was evident even at low temperatures, immediately following overnight dissolution in aqueous media in the refrigerator (Fig. 8). Upon heating, these transparent gels turned opaque. The only exception was P5, which disassembled upon heating, as the polymer precipitated out of solution and was unable to form crosslinks. On the other hand, the formation of these hydrogels proved to be reversible when the vials were again equilibrated at 5 °C (Fig. 8).

This observation contrasts with previous studies on PDFEA–PEG–PDFEA polymers, where physical hydrogel formation occurred only above the T_{CP} at the corresponding polymer concentration [14,35]. Notably, the ability of these polymers to form hydrogels immediately upon dissolution at low temperatures may offer practical advantages in biomedical applications, such as extrusion-based 3D printing combined with cell encapsulation. This process is commonly performed using biopolymers like gelatin or alginate–Ca^{2+} systems. However, unlike gelatin, which liquefies at physiological temperatures due to its UCST behavior, or alginate–Ca^{2+}, which can be destabilized in the presence of monovalent ions like Na^+, the current system offers improved thermal and ionic stability for such processing [49].

3.6. ^{19}F relaxation properties, MRS, and MRI

The suitability of the developed polymers P3–P6 for ^{19}F-MRI was evaluated based on their fluorine content and MR relaxation properties. An effective ^{19}F-MRI tracer should contain a high density of magnetically equivalent fluorine atoms that are readily detectable in aqueous environments. In addition to fluorine content, relaxation properties—namely T_1 (spin–lattice relaxation time) and T_2 (spin–spin relaxation time)—play a crucial role in tracer performance. Ideally, T_1 should be as short as possible to reduce the repetition time between scans and shorten the overall imaging duration. However, for macromolecular systems, T_1 values tend to increase with viscosity and can reach the range of seconds, which may hinder efficient imaging. Conversely, T_2 is often very short in polymeric systems, especially in those containing trifluoromethyl groups, leading to a rapid signal decay and reduced detectability [50].

We assessed the relaxation properties of the polymers under different conditions—at 25 °C, 37 °C, and after addition of 10 mM H_2O_2 (Table 5) [44].

Table 5
^{19}F relaxation times of P3-P5 in a 9.4 T Magnetic Field at 25 and 37 °C.

Sample	Temperature (°C)	Oxidation state	T_1 (ms) (mean ± SD)	T_2 (ms) (mean ± SD)
P3	25	Reduced	395 ± 40	106 ± 16
P3	37	Reduced	456 ± 41	221 ± 23
P4	25	Reduced	378 ± 34	129 ± 18
P4	37	Reduced	439 ± 24	244 ± 24
P5	25	Reduced	400 ± 38	155 ± 21
P5	37	Reduced	461 ± 39	270 ± 26
P3	25	Oxidized	301 ± 37	108 ± 16
P3	37	Oxidized	362 ± 39	223 ± 23
P4	25	Oxidized	284 ± 30	130 ± 18
P4	37	Oxidized	345 ± 32	245 ± 24
P5	25	Oxidized	306 ± 35	157 ± 21
P5	37	Oxidized	367 ± 37	272 ± 26

The T_1 of all samples at 25 °C was similar, around 395 ± 40 ms. Upon heating, their T_1 increased by 61 ± 31 ms ($p = 0.056$, marginal significance). Moreover, the oxidation of samples decreased their relaxation time by 93 ± 32 ms ($p = 0.004$). These results are well in line with our previous reports on PDFEA copolymers, where increasing temperature increased their T_1 [46]. Regardless, all these relaxation times are properly suited for ^{19}F-MRI applications.

As for T_2 – here we observed two nearly equal populations of ^{19}F relaxations – fast and slow, which is again in line with our previous reports on PDFEA copolymers [14]. The fast-relaxing population has a relaxation time around 25 ms, which is too short for practical ^{19}F MRI tracers and so this population was investigated only to a minor extent. In turn, the slow-relaxing population was characterized by a relaxation of around 100 to 140 ms, in line with our previous reports on PDFEA copolymers. The increasing temperature significantly prolonged its T_2 relaxation by 115 ± 21 ms ($p = 1.4 \cdot 10^{-7}$). This could be due to the transformation of particles from spherical/cylindrical micelles into nanogels which reveals the advantage of nanogels for ^{19}F MRI applications. Additionally, sample oxidation had no significant effect on the samples' relaxation times ($p = 0.93$). Such long T_2 relaxation states (especially when heated to body temperature) are advantageous for ^{19}F-MRI, as the polymers provide copious MR signal for detection *in vivo*.

These results show that boronate comonomers can endow the polymers with ROS-responsiveness, without compromising their T_2 MR properties. In contrast, our previously described ferrocene-containing fluorinated polymers, whose T_2 relaxations were very short in both their oxidized and reduced states (usually within the range of 5 to 30 ms) [51,52]. Thus, boronate-based thermo- and ROS-responsive systems are particularly suitable as ^{19}F-MRI tracers.

Timing of the turbo spin echo sequence used for MR imaging was optimized with respect to relaxation times of ^{19}F. The total length of the sequence (given by repetition time and number of acquisitions) was set to fit to approximately 15 min, which is a reasonable time for future in vivo applications. ^{19}F-MR image colocalized with ^{1}H-MR image of three polymers (P3, P4, P5) at different concentrations is shown in Fig. 9. Signal to noise ratios (SNR) are listed in Table 6.

The acquired ^{19}F-MR images (shown in red) in Fig. 9, merged with ^{1}H-MR images (shown in grayscale), from aqueous solutions of P3-P5 polymers demonstrate that all our polymers could be visualized at concentrations as low as 1 wt%, confirming their suitability to serve as ^{19}F-MRI tracers.

3.7. In vitro cytocompatibility

Finally, the cytocompatibility of the selected polymers P3-P5 has been evaluated through *in vitro* cytotoxicity assays. Live/dead assays using Ca-AM/PI were preformed to quantify living and dead cells upon exposure to polymer solutions at varying polymer concentrations (0.25, 0.5, and 1 mg/mL) over different time points (days 1, 3 and 7). Non-fluorescent Ca-AM converts into fluorescent calcein dye by intracellular esterase activity in living cells, which exhibits a bright green color upon binding to intracellular Ca^{2+} ions. While this conversion allows the dye to be retained within the cytoplasm of living cells, dead cells with compromised membranes do not retain calcein. In contrast, PI is cell-membrane impermeant and cannot enter living cells with intact membranes. It is a nucleic acid intercalating dye that binds to DNA of dead cells and manifests a bright red color. Fig. S24 displays the living and dead cells together for P3-P5 with respect to the control group. Using ImageJ software, these images were separated into red and green channels to count the living and dead cells. Cell viabilities were calculated as the ratio between the number of living cells and the total number of cells (Fig. S25). An initial decrease in cell viability observed on day 1 (Fig. S21) can likely be attributed to mild autofluorescence of the polymers overlapping with PI, temporarily affecting the live/dead readouts until protocol adjustments were implemented at later time

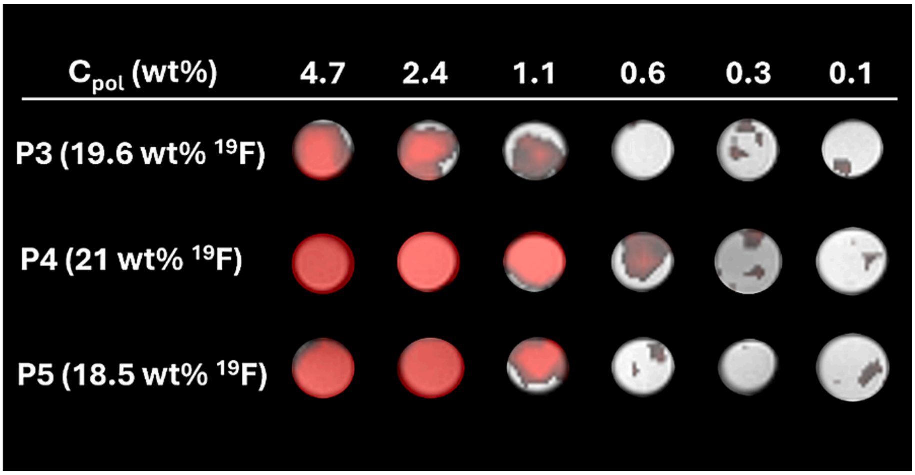

Fig. 9. Merge of ^{1}H-MRI (grayscale) and ^{19}F-MRI (red) of PBS solutions (140 mM, pH 7.4) corresponding to P3-P5 phantoms (plastic containers with a volume of 250 μL) at various polymer concentrations. (For interpretation of the references to color in this figure legend, the reader is referred to the web version of this article.)

Table 6
SNR of the ^{19}F signal of P3, P4, and P5 polymers at different polymer concentrations in PBS. Only SNR values above 2 are listed.

C_{pol} (wt%)	P3	P4	P5
4.7	4.2	13.9	6.5
2.4	3.6	10.1	6.4
1.1	2.1	5.9	3.5
0.6	<2	2,1	<2
0.3	<2	<2	<2
0.1	<2	<2	<2

points. At the end, we can show that all polymers at all concentrations displayed high cell viabilities after 3 days (cell viability > 89 %) and 7 days (cell viability > 84 %) without showing cytotoxicity, highlighting their potential for biomedical applications.

4. Conclusions

In this study, we designed and synthesized a range of BAB triblock copolymers where the B block is a statistical ROS- and thermoresponsive copolymer of DFEA and ROSm, and the A block is a hydrophilic PEtOx block. These copolymers self-assemble into nanoparticles upon dissolution in aqueous media and can physically crosslink into hydrogels at higher polymer concentrations. While the DFEA blocks enables detectability through ^{19}F-MRI for diagnostic purposes, ROSm units facilitate ROS-responsive particle disassembly, enabling controlled release at tumor sites. We prepared six triblock copolymers targeting two different hydrophilic-to-hydrophobic block ratios (1:2 and 1:4), since a low A/B ratio promotes physically crosslinked hydrogel formation from thermoresponsive triblock copolymers.

We studied the temperature-responsive self-assembly behavior of all particle systems and determined T_{CP1} and T_{CP2}, which describe the transformation temperature leading to nanoparticle formation and the critical temperature leading to aggregation, respectively. Based on this analysis, we excluded three polymers that exhibited T_{CP2} below 37 °C, as they would be unfit to serve biomedical applications, and further characterized the nanoparticle systems exploiting polymers P3, P4 and P5 (1 mg/mL in PBS) at body temperature. Even though P5 also exhibited particle instability starting at 37 °C, we investigated this nanoparticle system further based on the turbidimetry analysis. Nanogels formed by P5 led to physically crosslinked hydrogels at higher polymer concentrations, which can be of importance for several biomedical applications. DLS and SLS studies revealed that P3, P4, and P5 undergo particle type transformation from spherical/cylindrical nanostructures into nanogels with increasing temperature. When these systems were evaluated via ^{19}F-NMR, we showed that this transformation prolongs the T_2 relaxation times, improving the suitability for ^{19}F-MRI. Besides their potential as nanoparticle systems, we have shown that P3 and P4 formed physically-crosslinked hydrogels at high polymer concentration (40 wt%) even below and above their T_{CP1}, a property that can offer advantages for cell encapsulation.

When the ROS-responsive behavior of nanogels from P3, P4 and P5 was studied with DLS, it was shown that all systems displayed responsivity to H_2O_2 concentrations ranging between 0.4–2 mM, which coincide with levels of oxidative stress observed in tumors or in their vicinity. Furthermore, ^{19}F-NMR studies showed that the oxidation does not affect the relaxation times, which in turn does not impair the detectability of these particle systems for ^{19}F-MRI. The novelty of this system lies in the use of PDFEA, a ^{19}F-active thermoresponsive monomer, in combination with the boronate-based ROS responsive monomer, leading to a significant improvement of ^{19}F MRI properties compared to our previous study involving ferrocene as the ROS-sensitive switch [52]. Finally, cytocompatibility of nanogels of P3, P4, and P5 was confirmed via live/dead assays.

CRediT authorship contribution statement

Fatma Nalan Cetin: Writing – original draft, Visualization, Validation, Resources, Project administration, Methodology, Investigation, Formal analysis, Data curation, Conceptualization. **Zulfiya Cernochova:** Visualization, Supervision, Software, Resources, Methodology, Investigation, Formal analysis, Data curation. **Edward Vermeersch:** Investigation, Formal analysis, Data curation. **Vit Herynek:** Resources, Methodology, Investigation, Formal analysis, Data curation. **Ondrej Groborz:** Methodology, Investigation, Formal analysis, Data curation. **Ewa Pavlova:** Methodology, Investigation, Formal analysis, Data curation. **Miroslav Slouf:** Supervision, Methodology, Investigation, Funding acquisition, Formal analysis, Data curation. **Martin Hruby:** Writing – review & editing, Supervision, Resources, Project administration, Funding acquisition. **Arn Mignon:** Writing – review & editing, Validation, Supervision, Resources, Project administration, Funding acquisition, Conceptualization. **Richard Hoogenboom:** Writing – review & editing, Supervision, Resources, Project administration, Funding acquisition. **Sandra Van Vlierberghe:** Writing – review & editing, Validation, Supervision, Resources, Project administration, Funding acquisition, Conceptualization. **Kristyna Kolouchova:** Writing – review & editing, Validation, Supervision, Resources, Project administration, Funding acquisition, Conceptualization.

Declaration of competing interest

The authors declare that they have no known competing financial interests or personal relationships that could have appeared to influence the work reported in this paper.

Acknowledgements

This study was funded by Research Foundation Flanders (FWO) (G075621N, 1SC1225N, and K215824N).

K.K. gratefully acknowledges the financial support provided by Research Foundation – Flanders (FWO, Fonds Wetenschappelijk Onderzoek – Vlaanderen, project no. 1229422N and 1247425N).

OG and KK gratefully acknowledge the co-funding of this project from the Grant Agency of Charles University (GA UK), project No. 199125.

Z.C. and M.H. thank to the Ministry of Education, Youth and Sports of the Czech Republic (grant # LM2023053 EATRIS-CZ) and to the Ministry of Health of the Czech Republic (grant # NW24-03-00387). The study was co-funded by project New Technologies for Translational Research in Pharmaceutical Sciences/NETPHARM, project ID CZ.02.01.01/00/22_008/0004607, co-funded by the European Union.

The authors thank Dr. Victor R. de la Rosa for assistance with the synthesis of the PEtOx macroCTA.

Appendix A. Supplementary data

Supplementary data to this article can be found online at https://doi.org/10.1016/j.eurpolymj.2025.114211.

Data availability

The research data are available in Electronic Supporting Information and online repository: Data repository.

References

[1] F. Alexis, J.N. Anker, Theranostic nanotechnologies: moving beyond imaging drug localization? Ther. Deliv. 5 (2) (2014) 97–100, https://doi.org/10.4155/tde.13.136.

[2] Chen, X.; Wong, S. T. C. Cancer Theranostics. In *Cancer Theranostics*; Elsevier, 2014; pp 3–8. https://doi.org/10.1016/B978-0-12-407722-5.00001-3.

[3] S.M. Hosseini, J. Mohammadnejad, S. Salamat, Z. Beiram Zadeh, M. Tanhaei, S. Ramakrishna, Theranostic polymeric nanoparticles as a new approach in cancer therapy and diagnosis: a review, Mater. Today Chem. 29 (2023) 101400, https://doi.org/10.1016/j.mtchem.2023.101400.

[4] F. Chapelin, C.M. Capitini, E.T. Ahrens, Fluorine-19 MRI for detection and quantification of immune cell therapy for cancer, J. Immunother. Cancer 6 (1) (2018) 105, https://doi.org/10.1186/s40425-018-0416-9.

[5] J.C. Knight, P.G. Edwards, S.J. Paisey, Fluorinated contrast agents for magnetic resonance imaging; a review of recent developments, RSC Adv. 1 (8) (2011) 1415, https://doi.org/10.1039/c1ra00627d.

[6] L. Jaimes-Aguirre, B. Vianey Gibbens-Bandala, E. Morales-Avila, B. Eli Ocampo-García, M. Seyedeh-Fatemeh, A. Amirhosein, Polymer-based drug delivery systems, development and pre-clinical status, Curr. Pharm. Des. 22 (19) (2016) 2886–2903, https://doi.org/10.2174/1381612822666160217125028.

[7] J. Wahsner, E.M. Gale, A. Rodríguez-Rodríguez, P. Caravan, Chemistry of MRI contrast agents: current challenges and new frontiers, Chem. Rev. 119 (2) (2019) 957–1057, https://doi.org/10.1021/acs.chemrev.8b00363.

[8] R.F. Code, J.E. Harrison, K.G. Mcneill, M. Szyjkowski, In *vivo* ^{19} f spin relaxation in index finger bones, Magn. Reson. Med. 13 (3) (1990) 358–369, https://doi.org/10.1002/mrm.1910130303.

[9] O. Maxouri, Z. Bodalal, M. Daal, S. Rostami, I. Rodriguez, L. Akkari, M. Srinivas, R. Bernards, R. Beets-Tan, How to 19F MRI: applications technique, and getting started, Bjr|open 5 (1) (2023), https://doi.org/10.1259/bjro.20230019.

[10] K. Kolouchova, D. Jirak, O. Groborz, O. Sedlacek, N. Ziolkowska, M. Vit, E. Sticova, A. Galisova, P. Svec, J. Trousil, M. Hajek, M. Hruby, Implant-forming polymeric 19F MRI-tracer with tunable dissolution, J. Control. Release 327 (2020) 50–60, https://doi.org/10.1016/j.jconrel.2020.07.026.

[11] D. Jirak, A. Galisova, K. Kolouchova, D. Babuka, M. Hruby, Fluorine polymer probes for magnetic resonance imaging: quo vadis? MAGMA 32 (1) (2019) 173–185, https://doi.org/10.1007/s10334-018-0724-6.

[12] D. Babuka, K. Kolouchova, O. Groborz, Z. Tosner, A. Zhigunov, P. Stepanek, M. Hruby, Internal structure of thermoresponsive physically crosslinked nanogel of poly[n-(2-hydroxypropyl)methacrylamide]-block-poly[n-(2,2-difluoroethyl) acrylamide], prominent 19f mri tracer, Nanomaterials 10 (11) (2020) 2231, https://doi.org/10.3390/nano10112231.

[13] V. Herynek, M. Martinisková, Y. Bobrova, A. Gálisová, J. Kotek, P. Hermann, F. Koucký, D. Jirák, M. Hájek, Low-molecular-weight paramagnetic 19f contrast agents for fluorine magnetic resonance imaging, MAGMA 32 (1) (2019) 115–122, https://doi.org/10.1007/s10334-018-0721-9.

[14] K. Kolouchova, O. Groborz, M. Slouf, V. Herynek, L. Parmentier, D. Babuka, Z. Cernochova, F. Koucky, O. Sedlacek, M. Hruby, R. Hoogenboom, S. Van Vlierberghe, Thermoresponsive triblock copolymers as widely applicable ^{19} F magnetic resonance imaging tracers, Chem. Mater. 34 (24) (2022) 10902–10916, https://doi.org/10.1021/acs.chemmater.2c02589.

[15] K. Kolouchova, Z. Cernochova, O. Groborz, V. Herynek, F. Koucky, R. Jaksa, J. Benes, M. Slouf, M. Hruby, Multiresponsive fluorinated polymers as a theranostic platform using 19F MRI, Eur. Polym. J. 175 (2022) 111381, https://doi.org/10.1016/j.eurpolymj.2022.111381.

[16] O. Sedlacek, D. Jirak, A. Galisova, E. Jager, J.E. Laaser, T.P. Lodge, P. Stepanek, M. Hruby, ^{19} F magnetic resonance imaging of injectable polymeric implants with multiresponsive behavior, Chem. Mater. 30 (15) (2018) 4892–4896, https://doi.org/10.1021/acs.chemmater.8b02115.

[17] K. Kolouchová, V. Lobaz, H. Beneš, V.R. de la Rosa, D. Babuka, P. Švec, P. Černoch, M. Hrubý, R. Hoogenboom, P. Štěpánek, O. Groborz, Thermoresponsive properties of polyacrylamides in physiological solutions, Polym. Chem. 12 (35) (2021) 5077–5084, https://doi.org/10.1039/D1PY00843A.

[18] S.A.A. Rizvi, A.M. Saleh, Applications of nanoparticle systems in drug delivery technology, Saudi Pharmaceutical Journal 26 (1) (2018) 64–70, https://doi.org/10.1016/j.jsps.2017.10.012.

[19] M. Pitorre, H. Gondé, C. Haury, M. Messous, J. Poilane, D. Boudaud, E. Kanber, G. A. Rossemond Ndombina, J.-P. Benoit, G. Bastiat, Recent advances in nanocarrier-loaded gels: which drug delivery technologies against which diseases? J. Control. Release 266 (2017) 140–155, https://doi.org/10.1016/j.jconrel.2017.09.031.

[20] J. Wu, The enhanced permeability and retention (epr) effect: the significance of the concept and methods to enhance its application, J Pers Med 11 (8) (2021) 771, https://doi.org/10.3390/jpm11080771.

[21] F. Weinberg, N. Ramnath, D. Nagrath, Reactive oxygen species in the tumor microenvironment: an overview, Cancers (Basel) 11 (8) (2019) 1191, https://doi.org/10.3390/cancers11081191.

[22] V. Aggarwal, H. Tuli, A. Varol, F. Thakral, M. Yerer, K. Sak, M. Varol, A. Jain, Md. Khan, G. Sethi, Role of reactive oxygen species in cancer progression: molecular mechanisms and recent advancements, Biomolecules 9 (11) (2019) 735, https://doi.org/10.3390/biom9110735.

[23] C. de Gracia Lux, S. Joshi-Barr, T. Nguyen, E. Mahmoud, E. Schopf, N. Fomina, A. Almutairi, Biocompatible polymeric nanoparticles degrade and release cargo in response to biologically relevant levels of hydrogen peroxide, J. Am. Chem. Soc. 134 (38) (2012) 15758–15764, https://doi.org/10.1021/ja303372u.

[24] G.T. Kozma, T. Shimizu, T. Ishida, J. Szebeni, Anti-PEG antibodies: properties, formation, testing and role in adverse immune reactions to PEGylated nano-biopharmaceuticals, Adv. Drug Deliv. Rev. 154–155 (2020) 163–175, https://doi.org/10.1016/j.addr.2020.07.024.

[25] R. Hoogenboom, The future of poly(2-Oxazoline)s, Eur. Polym. J. 179 (2022) 111521, https://doi.org/10.1016/j.eurpolymj.2022.111521.

[26] E. Haladjova, S. Rangelov, C. Tsvetanov, Thermoresponsive polyoxazolines as vectors for transfection of nucleic acids, Polymers (basel) 12 (11) (2020) 2609, https://doi.org/10.3390/polym12112609.

[27] T. Lorson, M.M. Lübtow, E. Wegener, M.S. Haider, S. Borova, D. Nahm, R. Jordan, M. Sokolski-Papkov, A.V. Kabanov, R. Luxenhofer, Poly(2-Oxazoline)s based biomaterials: a comprehensive and critical update, Biomaterials 178 (2018) 204–280, https://doi.org/10.1016/j.biomaterials.2018.05.022.

[28] E. Jäger, V. Sincari, L.J.C. Albuquerque, A. Jäger, J. Humajova, J. Kucka, J. Pankrac, P. Paral, T. Heizer, O. Janouskova, R. Konefał, E. Pavlova, O. Sedlacek, F.C. Giacomelli, P. Pouckova, L. Sefc, P. Stepanek, M. Hruby, Reactive oxygen species (ROS)-responsive polymersomes with site-specific chemotherapeutic delivery into tumors via spacer design chemistry, Biomacromolecules 21 (4) (2020) 1437–1449, https://doi.org/10.1021/acs.biomac.9b01748.

[29] J. Jakeš, Regularized positive exponential sum (REPES) program - a way of inverting laplace transform data obtained by dynamic light scattering, Collect. Czechoslov. Chem. Commun. 60 (11) (1995) 1781–1797, https://doi.org/10.1135/cccc19951781.

[30] I. Ivanko, A. Mahun, L. Kobera, Z. Černochová, E. Pavlova, P. Toman, Z. Pientka, P. Štěpánek, E. Tomšík, Synergy between the assembly of individual PEDOT chains and their interaction with light, Macromolecules 54 (22) (2021) 10321–10330, https://doi.org/10.1021/acs.macromol.1c01975.

[31] Q. Zhang, C. Weber, U.S. Schubert, R. Hoogenboom, Thermoresponsive polymers with lower critical solution temperature: from fundamental aspects and measuring techniques to recommended turbidimetry conditions, Mater. Horiz. 4 (2) (2017) 109–116, https://doi.org/10.1039/C7MH00016B.

[32] M. Štěpánek, J. Hajduová, K. Procházka, M. Šlouf, J. Nebesářová, G. Mountrichas, C. Mantzaridis, S. Pispas, Association of poly(4-hydroxystyrene)- *block* -poly (ethylene oxide) in aqueous solutions: block copolymer nanoparticles with intermixed blocks, Langmuir 28 (1) (2012) 307–313, https://doi.org/10.1021/la203946s.

[33] Z. Černochová, V. Lobaz, L. Čtveráčková, P. Černoch, M. Šlouf, M. Filipová, M. Hrubý, J. Pánek, Encapsulating melittin from animal venom by finely tuned charge compensation with polymer carriers, Eur. Polym. J. 190 (2023) 111996, https://doi.org/10.1016/j.eurpolymj.2023.111996.

[34] M.D. Abramoff, P.J. Magalhaes, S.J. Ram, Image processing with image, J. Biophotonics Int. 11 (7) (2004) 36–42.

[35] B.D. Monnery, R. Hoogenboom, Thermoresponsive hydrogels formed by poly(2-oxazoline) triblock copolymers, Polym. Chem. 10 (25) (2019) 3480–3487, https://doi.org/10.1039/C9PY00300B.

[36] J.T. Lai, D. Filla, R. Shea, Functional polymers from novel carboxyl-terminated trithiocarbonates as highly efficient RAFT agents, Macromolecules 35 (18) (2002) 6754–6756, https://doi.org/10.1021/ma020362m.

[37] R. Marín, C. Abad, D. Rojas, D.I. Chiarello, T.-G. Alejandro, Biomarkers of Oxidative Stress and Reproductive Complications (2023) 157–233, https://doi.org/10.1016/bs.acc.2022.11.004.

[38] F.N. Cetin, A. Mignon, S. Van Vlierberghe, K. Kolouchova, Polymer- and lipid-based nanostructures serving wound healing applications: a review, Adv. Healthc. Mater. 14 (1) (2025), https://doi.org/10.1002/adhm.202402699.

[39] M.E. Fox, F.C. Szoka, J.M.J. Fréchet, Soluble polymer carriers for the treatment of cancer: the importance of molecular architecture, Acc. Chem. Res. 42 (8) (2009) 1141–1151, https://doi.org/10.1021/ar900035f.

[40] P.H.M. Van Steenberge, B. Verbraeken, M.-F. Reyniers, R. Hoogenboom, D. R. D'hooge, Model-based visualization and understanding of monomer sequence formation in gradient copoly(2-oxazoline)s on the basis of 2-methyl-2-oxazoline and 2-phenyl-2-oxazoline, Macromolecules 48 (21) (2015) 7765–7773, https://doi.org/10.1021/acs.macromol.5b01642.

[41] R.R. Taribagil, M.A. Hillmyer, T.P. Lodge, Hydrogels from ABA and ABC triblock polymers, Macromolecules 43 (12) (2010) 5396–5404, https://doi.org/10.1021/ma100464z.

[42] S. Cui, L. Yu, J. Ding, Thermogelling of amphiphilic block copolymers in water: ABA type versus AB or BAB type, Macromolecules 52 (10) (2019) 3697–3715, https://doi.org/10.1021/acs.macromol.9b00534.

[43] A.P. Constantinou, L. Wang, S. Wang, T.K. Georgiou, Thermoresponsive block copolymers of increasing architecture complexity: a review on structure–property relationships, Polym. Chem. 14 (3) (2023) 223–247, https://doi.org/10.1039/D2PY01097F.

[44] R. Kotha, D.D. Kara, R. Roychowdhury, K. Tanvi, M. Rathnanand, Polymersomes based versatile nanoplatforms for controlled drug delivery and imaging, Adv Pharm Bull 13 (2) (2023) 218–232. https://doi.org/10.34172/apb.2023.028.

[45] R. Hoogenboom, H. Schlaad, Thermoresponsive poly(2-oxazoline)s, polypeptoids, and polypeptides, Polym. Chem. 8 (1) (2017) 24–40, https://doi.org/10.1039/C6PY01320A.

[46] K. Kolouchova, O. Sedlacek, D. Jirak, D. Babuka, J. Blahut, J. Kotek, M. Vit, J. Trousil, R. Konefał, O. Janouskova, B. Podhorska, M. Slouf, M. Hruby, Self-assembled thermoresponsive polymeric nanogels for ^{19}F MR imaging, Biomacromolecules 19 (8) (2018) 3515–3524, https://doi.org/10.1021/acs.biomac.8b00812.

[47] D. Babuka, K. Kolouchova, M. Hruby, O. Groborz, Z. Tosner, A. Zhigunov, P. Stepanek, Investigation of the internal structure of thermoresponsive diblock poly(2-methyl-2-oxazoline)-b-poly[N-(2,2-difluoroethyl)acrylamide] copolymer nanoparticles, Eur. Polym. J. 121 (2019) 109306, https://doi.org/10.1016/j.eurpolymj.2019.109306.

[48] C. Dunnill, T. Patton, J. Brennan, J. Barrett, M. Dryden, J. Cooke, D. Leaper, N. T. Georgopoulos, Reactive oxygen species (ROS) and wound healing: the functional role of ROS and emerging ROS-modulating technologies for augmentation of the healing process, Int. Wound J. 14 (1) (2017) 89–96, https://doi.org/10.1111/iwj.12557.

[49] H. Kim, C. Bae, Y.-M. Kook, W.-G. Koh, K. Lee, M.H. Park, Mesenchymal stem cell 3D encapsulation technologies for biomimetic microenvironment in tissue regeneration, Stem Cell Res Ther 10 (1) (2019) 51, https://doi.org/10.1186/s13287-018-1130-8.

[50] D. Havlicek, V.M. Panakkal, L. Voska, O. Sedlacek, D. Jirak, Self-assembled fluorinated nanoparticles as sensitive and biocompatible theranostic platforms for ^{19}F MRI, Macromol. Biosci. 24 (6) (2024), https://doi.org/10.1002/mabi.202300510.

[51] K. Kolouchova, O. Groborz, Z. Cernochova, A. Skarkova, J. Brabek, D. Rosel, P. Svec, Z. Starcuk, M. Slouf, M. Hruby, Thermo- and ROS-responsive self-assembled polymer nanoparticle tracers for ^{19}F MRI theranostics, Biomacromolecules 22 (6) (2021) 2325–2337, https://doi.org/10.1021/acs.biomac.0c01316.

[52] P. Švec, O.V. Petrov, J. Lang, P. Štěpnička, O. Groborz, D. Dunlop, J. Blahut, K. Kolouchová, L. Loukotová, O. Sedláček, T. Heizer, Z. Tošner, M. Šlouf, H. Beneš, R. Hoogenboom, M. Hrubý, Fluorinated ferrocene moieties as a platform for redox-responsive polymer ^{19}F MRI theranostics, Macromolecules 55 (2) (2022) 658–671, https://doi.org/10.1021/acs.macromol.1c01723.